JGR Solid Earth

RESEARCH ARTICLE
10.1029/2021JB021845

Topographic Amplification of Crustal Subsidence by the Rainwater Load of the 2019 Typhoon Hagibis in Japan

Wei Zhan[1,2], **Kosuke Heki**[2], **Syachrul Arief**[2,3], **and Mizuki Yoshida**[2,4]

[1]The First Monitoring and Application Center, China Earthquake Administration, Tianjin, China, [2]Department of Earth and Planetary Sciences, Hokkaido University, Sapporo, Japan, [3]Geospatial Information Authority, Cibinong, Indonesia, [4]Kiso-Jiban Consultants Co. Ltd, Tokyo, Japan

Key Points:

- We estimate water vapor distribution in the 2019 super typhoon Hagibis with a dense GNSS network in Japan and compare it with precipitation
- We estimate the distribution of rainwater load by the typhoon using the observed crustal subsidence, which exceeds the total precipitation
- The discrepancy possibly reflects the amplification of subsidence due to selective deployment of the GNSS stations in concave terrains

Supporting Information:

Supporting Information may be found in the online version of this article.

Correspondence to:

W. Zhan and K. Heki,
zw000373@163.com;
heki@sci.hokudai.ac.jp

Citation:

Zhan, W., Heki, K., Arief, S., & Yoshida, M. (2021). Topographic amplification of crustal subsidence by the rainwater load of the 2019 typhoon Hagibis in Japan. *Journal of Geophysical Research: Solid Earth, 126*, e2021JB021845. https://doi.org/10.1029/2021JB021845

Received 10 FEB 2021
Accepted 12 MAY 2021

Abstract The super typhoon Hagibis traveled northeastward through eastern Honshu, Japan, causing disastrous heavy rainfalls along its path on October 11 and 12, 2019. We performed a comprehensive space geodetic study of water brought by this typhoon using a dense network of Global Navigation Satellite System (GNSS) receivers in Japan. First, we studied the time evolution of altitude-corrected precipitable water vapor field and compare the movement of water vapor centroid with the rain distribution from radar rain gauge analyzed precipitation. The total amount of water vapor derived by spatially integrating precipitable water vapor on land remained steady at ~20 Gt. The total precipitation by this typhoon was ~92, and ~33 Gt of it fell onto the land area of eastern Honshu. Next, we studied crustal subsidence caused by the typhoon rainwater as surface load. The GNSS stations located under the typhoon path temporarily subsided 1–2 cm on the landfall day and the subsidence mostly recovered on the next day. Using the vertical crustal movement data, we estimated the distribution of surface water in eastern Honshu assuming the layered spherical earth. The amount of the surface load on October 12 was ~71 Gt, which significantly exceeds the cumulative rainfall on land. We consider that the excess subsidence largely originates from the selective deployment of GNSS stations in the concave topography, for example, along valleys and within basins, in the mountainous Japanese Islands.

Plain Language Summary A tropical cyclone transports a large amount of sea water to land as water vapor. The water becomes a torrential downpour, and the rainwater temporarily staying on land depresses the solid earth as a load. We study the super typhoon Hagibis in 2019 October using a dense network of continuous global navigation satellite system (GNSS) stations in Japan as a sensor of both water vapor and ground subsidence. We first map the distribution of water vapor using the delays of microwave signals from the satellites during the typhoon passage. The water vapor centroid moved together with the precipitation centroid along the path of the eye of the typhoon. With a model describing crustal subsidence as a function of distance from a unit load, we can infer the total amount of rainwater on land. The estimated amount of rainwater, however, exceeded the cumulative rainfall on land. We consider this paradox caused by local-scale concentration of rainwater around the Japanese GNSS stations, which are deployed along valleys and within basins where rainwater gathers. This study would serve as a milestone to understand complicated crustal dynamics during heavy rains in mountainous countries.

1. Introduction

A category 5 super typhoon Hagibis, also known as the 2019 Typhoon No.19 in Japan, hit the Japanese Islands in October 2019. This typhoon made landfall in Central Japan around 9 UT on October 12, 2019 as one of the strongest typhoons of the century to hit the country and killed 91 people, damaged more than 85,000 homes and flooded dozens of rivers (Nippon Hoso Kyokai, 2019; Natsuaki & Nagai, 2020; Tay et al., 2020). Here, we comprehensively study this typhoon using the dense network of continuous receiving stations of Global Navigation Satellite System (GNSS) satellites in Japan.

The Japanese GNSS Earth Observation Network (GEONET) is run by Geospatial Information Authority (GSI), Japan, and is composed of ~1,300 ground GNSS stations (Tsuji & Hatanaka, 2018). Its main purpose is to monitor crustal deformation of tectonic origin, but it has also been used to measure precipitable water vapor (PWV). Since Bevis et al. (1992) showed the potential of GNSS receivers to sense atmospheric

water vapor, meteorological application of the Japanese dense GNSS network has been sought (e.g., Tsuda et al., 1998). Since 2009, PWV data from GNSS have been assimilated in the meso-scale model of the Japan Meteorological Agency (JMA) to improve weather forecast accuracy (e.g., Shoji, 2015). Recently, Arief and Heki (2020) used GEONET to study water vapor concentration along the stationary weather front in SW Japan, which often brings heavy rain disasters there. They found that the heavy rain episodes in the 2017–2019 summer there occurred when the water vapor concentration index (Shoji, 2015) and PWV, reduced to sea level, are high, using the GEONET data.

GNSS meteorology has been applied to study the troposphere during tropical cyclone passages. Graffigna et al. (2019) studied behaviors of atmospheric delay gradients during the 2017 Hurricane Harvey in North America, and Ejigu et al. (2020) studied PWV fields during the landfall of Hurricane Florence in North America in 2018 and compared them with the distribution of precipitation measured from satellite. It is not well understood, however, whether all the water is stored as water vapor in the sky or only a part of it stays in the troposphere serving as an ocean-to-land water pathway. Zhao et al. (2018) used 5-min PWV data derived from GNSS observations for the typhoon event that passed over Zhejiang Province, China, July 10–12, 2015 and demonstrated that their method could predict ~3/4 of precipitation events 10–30 min earlier than their onset with a false alarm rate <1/5.

GEONET has also been used to study crustal deformation by changes in seasonal surface loads such as snow and atmosphere (e.g., Heki, 2001, 2004) as well as those of tectonic origin. Huge amounts of rainwater causes crustal deformation. Milliner et al. (2018) studied vertical and horizontal crustal movements around the coast of the Gulf of Mexico, USA, over a 5-week period including the Hurricane Harvey landfall on August 26, 2017. They assumed elastic deformation caused by the surface water load and estimated the daily distribution of water using the three-dimensional displacements of GNSS stations. Inversion results showed the amount of surface water reaching the maximum of ~31 km^3 (1 km^3 rainwater corresponds to ~1 Gt) 5 days after the landfall, which corresponds to one third of the precipitation. They found that the storm water drained into ocean by ~8.2 km^3/day and was also lost by evapotranspiration over the following 5 weeks. Because the duration of the storm water staying on surface falls short of the time resolution of time-variable gravity measured by Gravity Recovery and Climate Experiment satellites (e.g., Wahr et al., 1998), crustal deformation plays the main role to study water dynamics by a tropical cyclone.

In this study, we perform a comprehensive space geodetic study of water brought by the typhoon Hagibis in order to understand the dynamic behavior of typhoon-origin water and water vapor in Japan. First, we recover altitude-corrected PWV distribution using the atmospheric delay gradient vectors estimated by the dense GNSS array GEONET. Then, we compare them with the precipitation during the typhoon based on precipitation data from JMA. We study vertical crustal movements associated with the water load brought by the typhoon, using the F5 solutions of the GEONET station coordinates from GSI (Takamatsu et al., 2020) and those from the Nevada Geodetic Laboratory, University of Nevada, Reno (UNR) (Blewitt et al., 2018). We then estimate the distribution of surface water using the crustal deformation data from GEONET assuming elastic response of lithosphere. Finally, we compare amounts of the surface water with the precipitation and discuss the behavior of the rainwater, for example, the time constant of the water drainage to ocean and the consistency of the amount of water from surface deformation with those by direct measurement of precipitation.

2. Data

2.1. Tropospheric Data From UNR

We use data from the dense GNSS network GEONET that has a typical inter-station separation of 15–30 km (Figure 1). The temporal resolution of tropospheric parameters in its official solution (F5 solution) is 1 h for zenith delays and 3 h for gradient vectors (Takamatsu et al., 2020). Because this is not sufficient to study dynamics of water vapor during a typhoon passage, we here use tropospheric delay data from the UNR database (Blewitt et al., 2018).

They estimated tropospheric parameters using the GIPSY/OASIS-II Version 6.1.1 software with the Precise Point Positioning (PPP) technique (Zumberge et al., 1997). They estimated the zenith wet delay (ZWD) and the atmospheric delay gradient vectors every 5 min following the 2010 IERS convention (Petit &

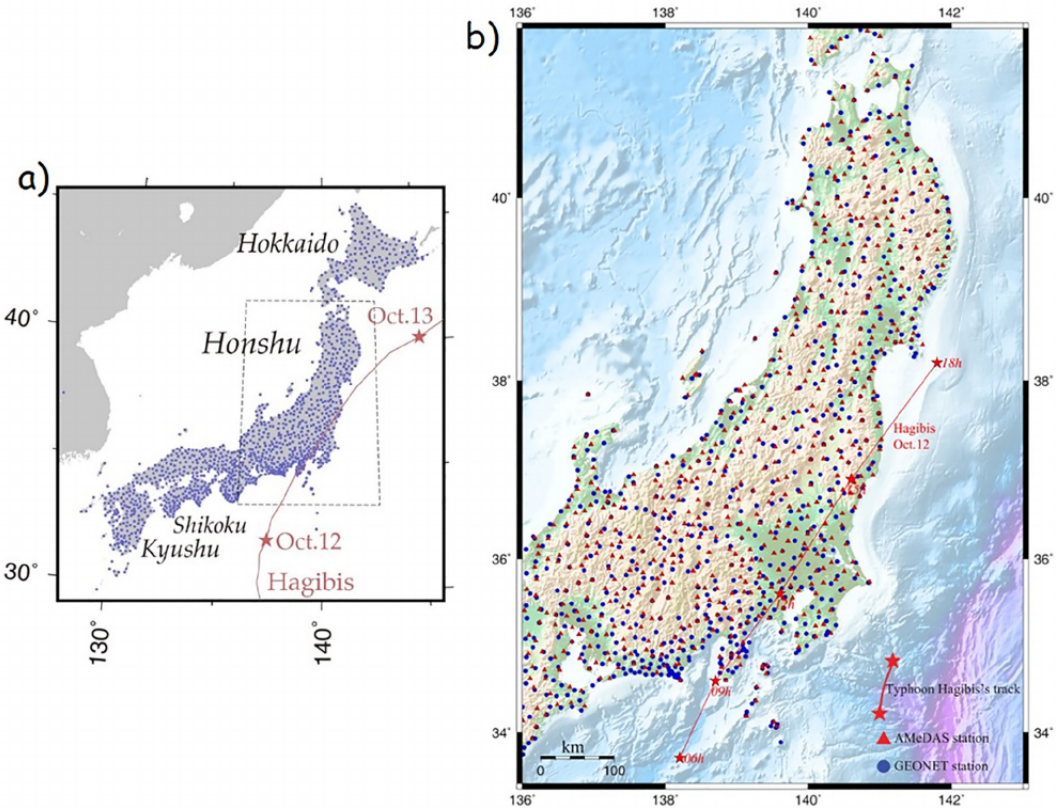

Figure 1. (a) Map of Japan and four major islands and GEONET GNSS stations (blue squares). (b) Close up view of eastern Honshu together with the GEONET (blue circle) and AMeDAS (red triangle) stations. Red curves and stars show the track of the typhoon Hagibis and the typhoon center positions at the epochs shown in UT (beginning of the day in (a)). AMeDAS, Automated Meteorological Data Acquisition System; GEONET, GNSS Earth Observation Network; GNSS, Global Navigation Satellite System.

Luzum, 2010) and using the ECMWF weather model (Simmons et al., 2007), the Vienna Mapping Function 1 (VMF1) (Böhm et al., 2006), and the tropospheric gradient model of Chen and Herring (1997). The data base also includes PWV derived by multiplying ZWD with a factor calculated using the average temperature of atmospheric water vapor.

A simple plot of PWV distribution does not reproduce real distribution of wet atmosphere, because water vapor stays in low troposphere and is much influenced by station elevations. In order to map wet atmosphere, we follow the method of Arief and Heki (2020) to reconstruct PWV reduced to sea-level by spatially integrating the delay gradient from the PWV at low elevation (e.g., coastal) stations.

There is one improvement from the original method by Arief and Heki (2020). Because the UNR data base used to include only zenith total delay (ZTD) and the delay gradients, Arief and Heki (2020) subtracted zenith hydrostatic delay calculated from surface pressure and converted ZWD to PWV. In 2019 fall, the UNR solution started to include PWV. It became unnecessary to derive PWV from ZTD, and we can directly put UNR products into the program to estimate altitude-corrected PWV. The dynamic behavior of water vapor during the typhoon Hagibis passage will be discussed in Section 3.1.

2.2. Radar Rain Gauge Analyzed Precipitation From JMA and Other Nongeodetic Data

Precipitation on the Japanese Islands is measured by the Automated Meteorological Data Acquisition System (AMeDAS) network of JMA, whose density is similar to GEONET (Figure 1b). Rain gauges in AMeDAS provide accurate rainfall data. However, they are sparse in mountain regions and may underestimate the total amount of typhoon rainfall that is often caused by winds blowing uphill in mountains. Rain radar, on the other hand, can estimate the two dimensional (2D) distribution of rainfall intensity although their data need to be calibrated by conventional rain gauge data. Here, we use the Radar Rain gauge Analyzed Precipitation (RRAP) data, made available by JMA taking advantage of the accurate but spatially sparse rain gauges and 2D radar observations with inherent ambiguities in absolute rain intensities. Time-variable distribution of heavy rain and total amount of rainwater will be discussed in Section 3.2 using such RRAP data.

We also use atmospheric surface pressure data from AMeDAS later to remove atmospheric load contributions to vertical crustal movements. Pressure changes at coastal stations during the typhoon passage are also compared with the tide gauge records to evaluate the degree of compensation of atmospheric pressure anomaly by changing sea levels. These issues are discussed in Section 4.2.

2.3. GNSS Station Position Time Series

First, we compare the two sets of the GEONET station coordinates, the F5 solution from GSI and the corrected F5 solution (F5c). The F5 solution (Takamatsu et al., 2020) is composed of daily station coordinates estimated with the Bernese software using final orbits of the satellites produced by International GNSS Service (IGS) and replaced the old F3 solution (Nakagawa et al., 2009) in April 2021. There, they estimate the positions relative to the reference station in Tsukuba, ~50 km northeast of Tokyo, whose position is determined relative to ~100 IGS stations distributed worldwide using the IGb14 reference frame. The interval of the estimation of ZTD and atmospheric delay gradients is 1 and 3 h, respectively, much improved from the 3 and 24 h in the F3 solution. They use the VMF1 atmospheric mapping function (Böhm et al., 2006).

To reduce common mode errors, we perform the following procedures. We first select ~100 stations evenly distributed in the country (first generation GEONET stations 0001–0099 installed in 1994) and defined the median coordinates over a 31 days period around October 12 (the typhoon landfall day) as the reference. For each of the 31 days, we estimate the 7 parameters of the Helmert transformation (3 translations, 3 rotations, and 1 scale change) to minimize the differences between the standard coordinates of the 100 standard stations and their observed coordinates. Then, we apply the daily Helmert transformation parameters to adjust the observed coordinate of all the stations. The corrected F5 solution (F5c) (Figure 2b) shows better repeatability than the original F5 solution (Figure 2a). In this study, we use F5c to study vertical crustal movement by the typhoon rain.

Another set used in this study is the daily position time series provided by UNR (Blewitt et al., 2018). Station coordinates are estimated every 24 h by applying the PPP method of the GIPSY/OASIS-II software package (Bertiger et al., 2020) in IGS14. We directly plot the daily vertical positions relative to the median without any correction (Figure 2c). Figure 2d shows that the F5c and UNR solutions of the 7 stations in Fukushima, NE Japan (Figure 2f), are well correlated.

Their between-software differences have root-mean-squares (RMS) of ~5 mm, which gives an idea of realistic accuracies of the daily vertical positions in these solutions. RMS decreases to 3 mm by taking the seven station averages (Figure 2e), suggesting validity of spatial smoothing to reduce random errors in station coordinates. Figure 2 shows that all the F5, F5c, and UNR solutions show significant subsidence on the typhoon landfall day (October 12, 2019), and there are no significant systematic inter-solution differences in the amount of the subsidence.

3. Results

3.1. Water Vapor in 2019 Typhoon Hagibis

Figure 3 shows the distribution of the altitude-corrected PWV at six epochs on October 11–12, 2019 together with the path of the typhoon Hagibis. They are reconstructed by spatially integrating the atmospheric

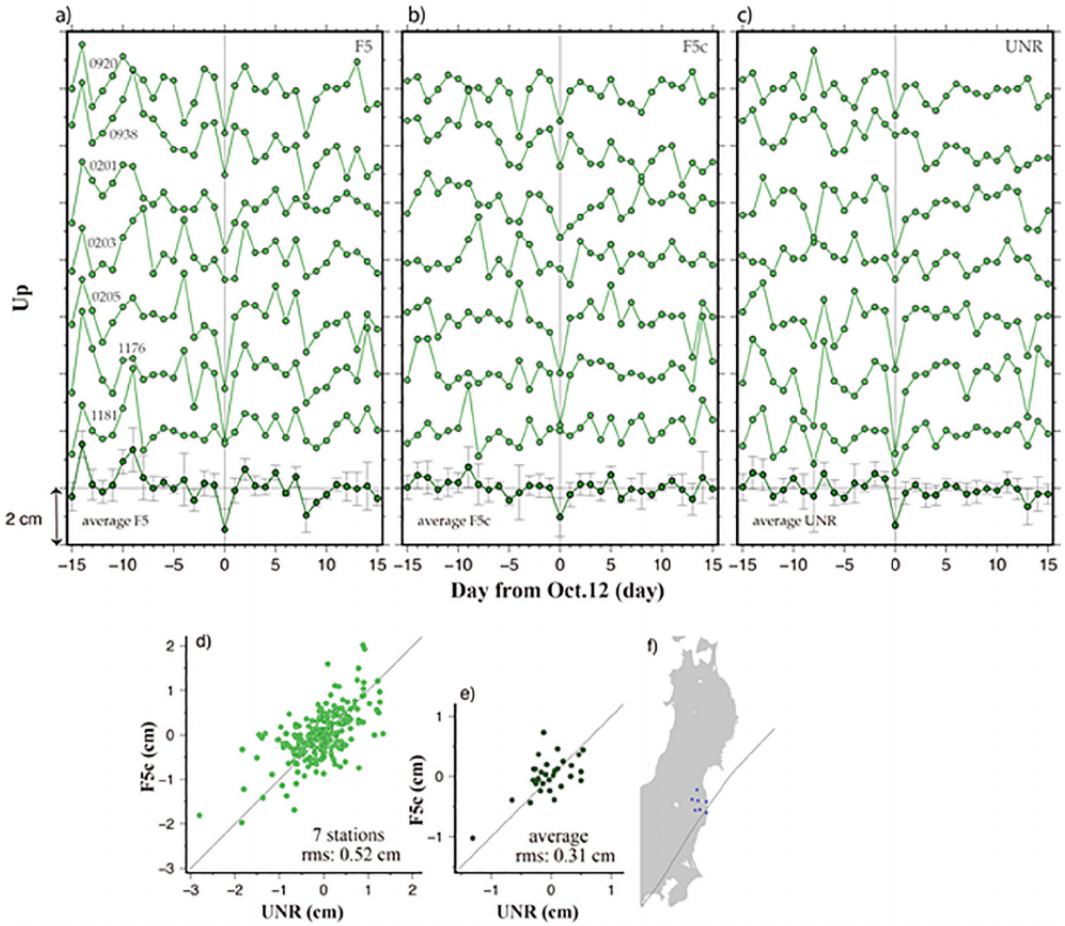

Figure 2. Panels (a)–(c) show vertical position time series relative to their median over time intervals of ±15 days (31 days) around the typhoon Hagibis landfall day, October 12, 2019. We show data from seven stations in Fukushima (f) along the typhoon path (gray line). Here, we compare the F5 solution (a) and the F5c solutions corrected for common mode errors (b), and the UNR solution (c). The F5c solutions (b) show better repeatability than F5 (a). At the lowermost part of (a)–(c), we show the average, together with the standard deviation, of the seven stations. In (d), we compare short-term vertical fluctuations between F5c and UNR solutions over 31 days for the 7 stations (217 points). They show RMS difference of ~5 mm, which is reduced to ~3 mm by taking the average positions of the seven stations (31 points) (e). RMS, root-mean-squares; UNR, University of Nevada, Reno.

delay gradient vectors and the PWV at low elevation stations. We use the algorithm developed by Arief and Heki (2020) with one difference in the procedure that we directly use PWV, made available in the UNR database from 2019, instead of ZWD in the original method (Arief & Heki, 2020).

As shown by reddish color in Figures 3a–3c, the atmosphere above the Japanese Islands was wet before the typhoon landfall. Extremely wet regions, shown in dark red, emerge along the southern coast of central Honshu as the typhoon approaches. This "red region" moves together with the center of the typhoon (Figure 3). Such a detailed map could not be drawn without GEONET considering that radiosondes, a conventional meteorological sensor of water vapor, are launched only twice a day at only ~10 observatories in Japan.

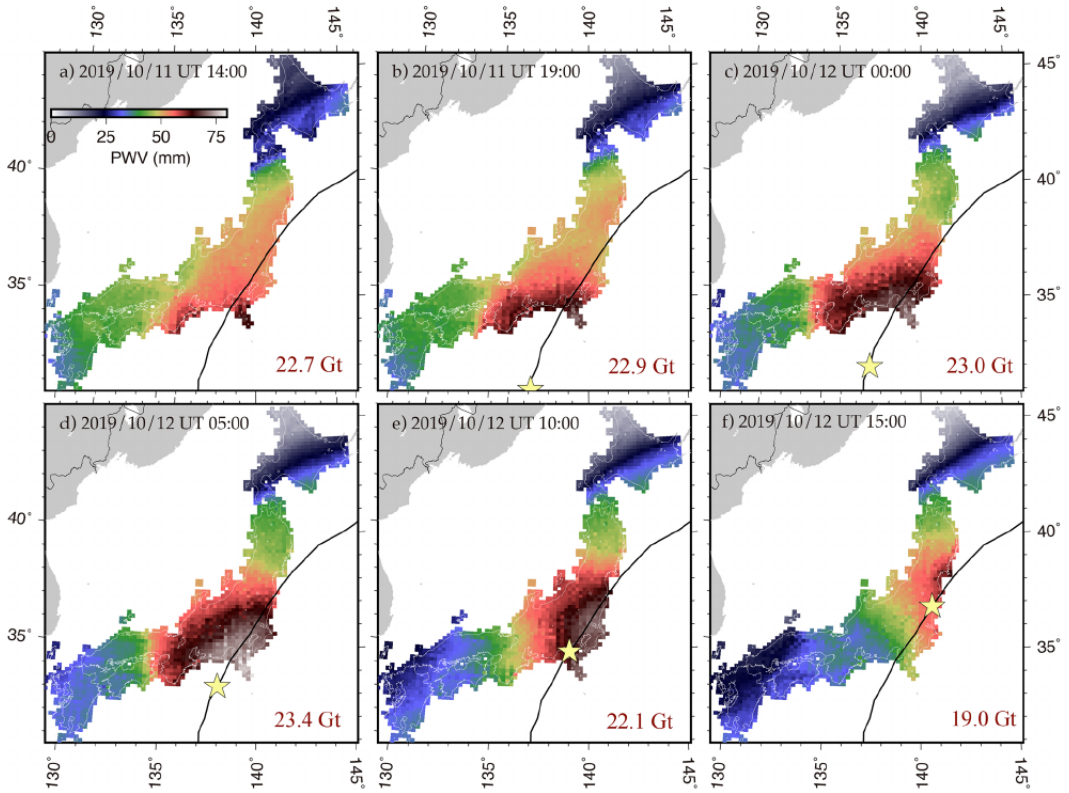

Figure 3. Altitude-corrected PWV calculated following Arief and Heki (2020) at six epochs with 5-h separation on October 11–12, 2019. Black curve shows the typhoon Hagibis track and the yellow stars indicate its center at these epochs. The typhoon Hagibis was above the land area during UT 9–15 on October 12. Total amounts of water calculated by horizontally integrating PWV above the land area are given at right-lower corner for these six epochs. PWV, precipitable water vapor.

It is straightforward to calculate total amount of water by spatially integrating PWV over the land area of the Japanese Islands. The integrated amounts of PWV were ~20 Gt at each of the six epochs shown in Figure 3 (a part it already changed into rainwater at these epochs). Because we cannot measure water vapor in oceanic areas, the difference between epochs would partly reflect the percentage of the overlap of the region rich in water vapor with the Japanese Islands and partly show the decay of the typhoon.

In a typhoon, water vapor supplied from sea surface by evaporation temporarily stays in the atmosphere and travels with the typhoon, causing delay of microwave signals from GNSS satellites. The amount of water vapor in a typhoon, ~20 Gt in the present case, corresponds to the capacity of a "bucket" to transport water from sea to land. Water in the bucket is constantly replenished from ocean as it goes out as rainwater. The size of the bucket is much less than the cumulative precipitation as discussed in the next section, and the amount of atmospheric water vapor would be governed by the balance of the input (from ocean) and the output (rain).

3.2. Precipitation During 2019 Typhoon Hagibis

RRAP provides distribution of accurate rain rate with high spatial resolution taking advantage of rain radar and conventional rain gauges. Figure 4 shows the amount of rainfall integrated over 1-hour periods

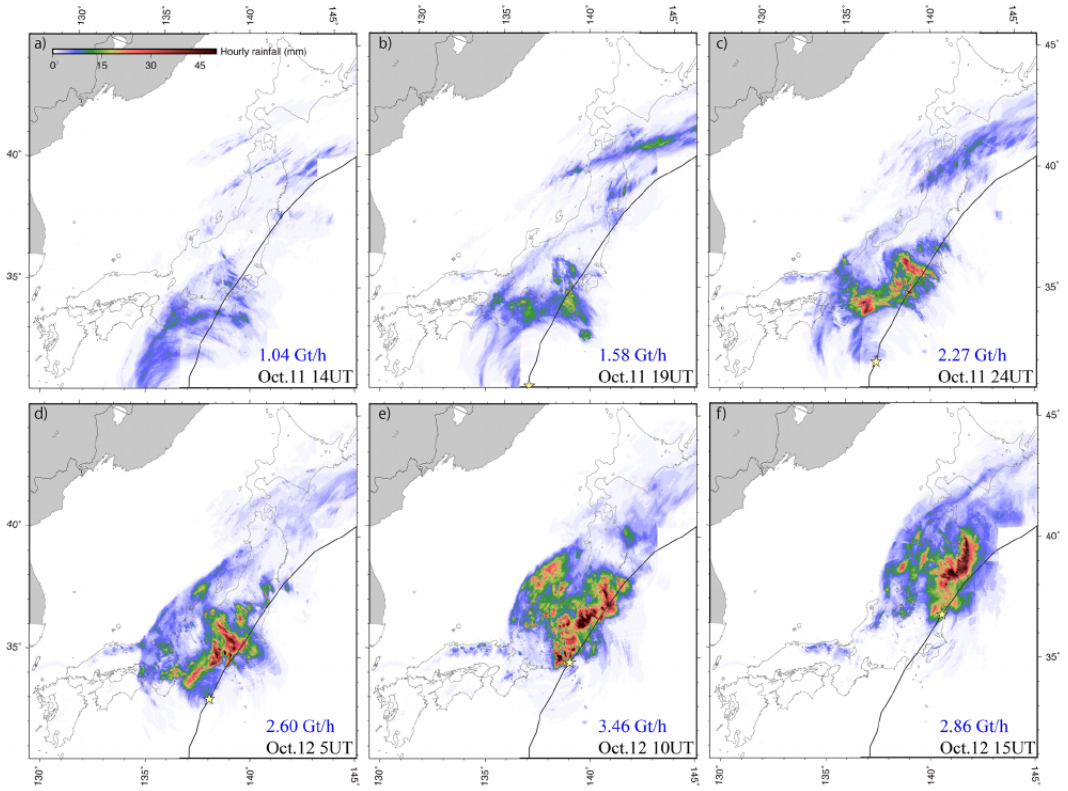

Figure 4. Distributions of hourly precipitation at the same six epochs (measured over 1 h periods preceding the epochs) shown for PWV in Figure 3. Black curves and yellow stars show the typhoon track and the typhoon center positions at the epochs. Spatially integrated hourly rainfalls (both land and ocean) are shown at the low-right corner for these six intervals. PWV, precipitable water vapor.

preceding the same six epochs as in Figure 3. Unlike water vapor, precipitation data cover the offshore area, within ~100 km from the coast. There was little rainfall on October 8–10 in eastern Honshu, and the rainfall on land by this typhoon started around 13 UT October 11 (Figure 4a), well before the typhoon landfall (~9 UT, October 12). Areas of strong rainfall roughly coincide with the "red region" (altitude-corrected PWV exceeding 50 mm) of water vapor in Figure 3. We spatially integrate the hourly rainfall fields over the whole region covered by the radar (both land and ocean) and the value ranges 1.0–3.5 Gt/hour for the periods in Figure 4. The total precipitation over 48 h covering October 11 and 12 exceeds 90 Gt, out of which ~33 Gt fell on the land area of eastern Honshu. They are significantly larger than the spatially integrated PWV (capacity of bucket), which implies that atmosphere merely serves as a pathway of water from ocean to land in a typhoon, that is, water vapor is constantly supplied from ocean and constantly consumed as rainfall.

Figure 5a compares the time series of spatially integrated precipitation and water vapor from GNSS-derived PWV estimates. The amount of water vapor stays high until ~6 UT on October 12. Shortly before the typhoon landfall, water vapor starts to decrease rapidly. On the other hand, typhoon precipitation starts around 1 UT, October 11, and the hourly rain keeps increasing for ~24 h. Water vapor is the maximum around the typhoon landfall time and rapidly decreases after that. PWV finally becomes as small as ~10 Gt, a standard value of total water vapor above the entire country in October.

The centroids of precipitation and atmospheric water vapor (Figure 5b) move northeastward in tandem along a path shifted northward from the typhoon path. Before the landfall, both centroids would be located

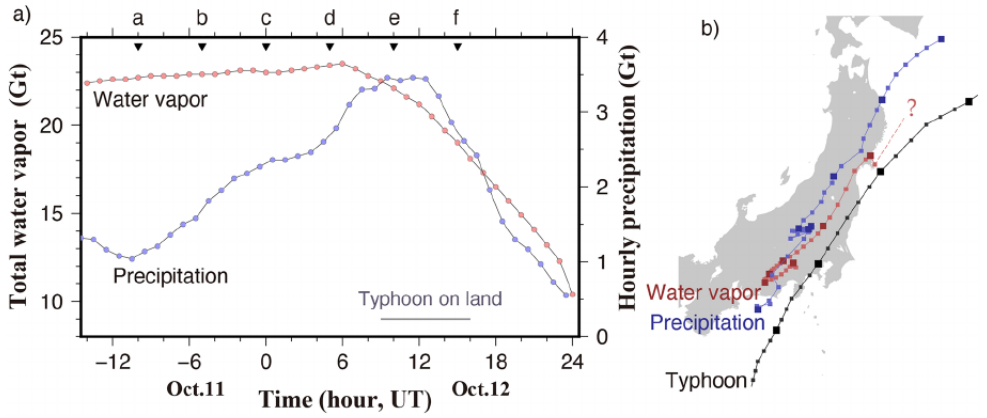

Figure 5. (a) We compare the time series of hourly precipitation over the whole region, including land and ocean, covered by the rain radar with the total amount of water vapor derived by spatially integrating PWV over the Japanese Islands. Water vapor started to decrease shortly before the typhoon landfall around nine on October12. Triangles marked a-f indicate the six epochs given in Figure 3. In (b), centroid (weighted mean position) of precipitation (blue) and water vapor (red) are compared with the typhoon path (black). These positions are given for the time interval shown in the time series in (a) (from 11 UT, October11, to 24 UT, October 12), and large symbols on the paths indicate 6-h time marks. Centroid of water vapor is derived as the weighted mean position of the area with PWV exceeding 50 mm (region shown with red color in Figure 3). No water vapor centroids are given after 19 UT, October 12 because the area with PWV > 50 mm on land disappeared after that. PWV, precipitable water vapor.

offshore, but we could not locate them correctly due to the lack of coverage of GNSS stations and rain radar in the ocean. After its landfall, the rain centroid moves along a path ~200 km north of the eye of the typhoon (Figure 5b). This is also obvious in Figure 4, that is, heavy rains occur mainly to the north of the eye of the typhoon. This would be due to wind direction and land-ocean distribution of the studied region, that is, strong wet landward winds at the northern side of the typhoon would have caused the heavy rain. The water vapor centroid is located between the typhoon center and the rain centroid. Its southward shift from the rain centroid of ~100 km would reflect the removal of water vapor from air in the heavy rain area by condensation.

3.3. Crustal Movement and Water Load by 2019 Typhoon Hagibis

Cumulative rain during the Typhoon Hagibis from 0:00 UT on October11 to 24:00 UT on October12, 2019 is ~92 Gt, and ~33 Gt of it fell onto the land region of eastern Honshu, covered by blocks for estimating surface load later in Section 4.2 (Figure 6). Because there are only insignificant rainfalls over a few days preceding this typhoon, rainwater brought by this typhoon would have depressed the ground as a load on October 12 as seen in Figure 2.

Figure 6 shows that heavy rainfalls occur in inland regions of the Kanto District, while rains concentrate along the Pacific coast in the central and northeast Honshu. Rivers in Japan are mostly short and steep due to its mountainous terrain, which allows the rainwater to quickly drain to the ocean. In Figure 6 inset, we show nine groups of GNSS stations, each group consisting of seven stations. Five of the groups, shown in blue, are located in flooded areas, and the rest, shown in green, are located in nonflooded areas. We will compare behaviors of these two groups.

In Figures 7a and 7c, we compare average time series of vertical crustal movements (F5c solution) from four unflooded and five flooded regions. The latter groups all show subsidence of 1–2 cm on the typhoon landfall day (October 12) relative to the median over the period ±15 days around October 12. The amounts of the subsidence exceed the noise level (the error bars reflect the scatter of seven stations within the groups) and are considered to show elastic response of the lithosphere to the rainwater load. The four nonflooded groups, on the other hand, do not exhibit clear subsidence on October 12 (Figure 7a). This is also confirmed by the distribution of subsidence shown in Figure 7b. The subsided areas, depicted as blue dots, roughly

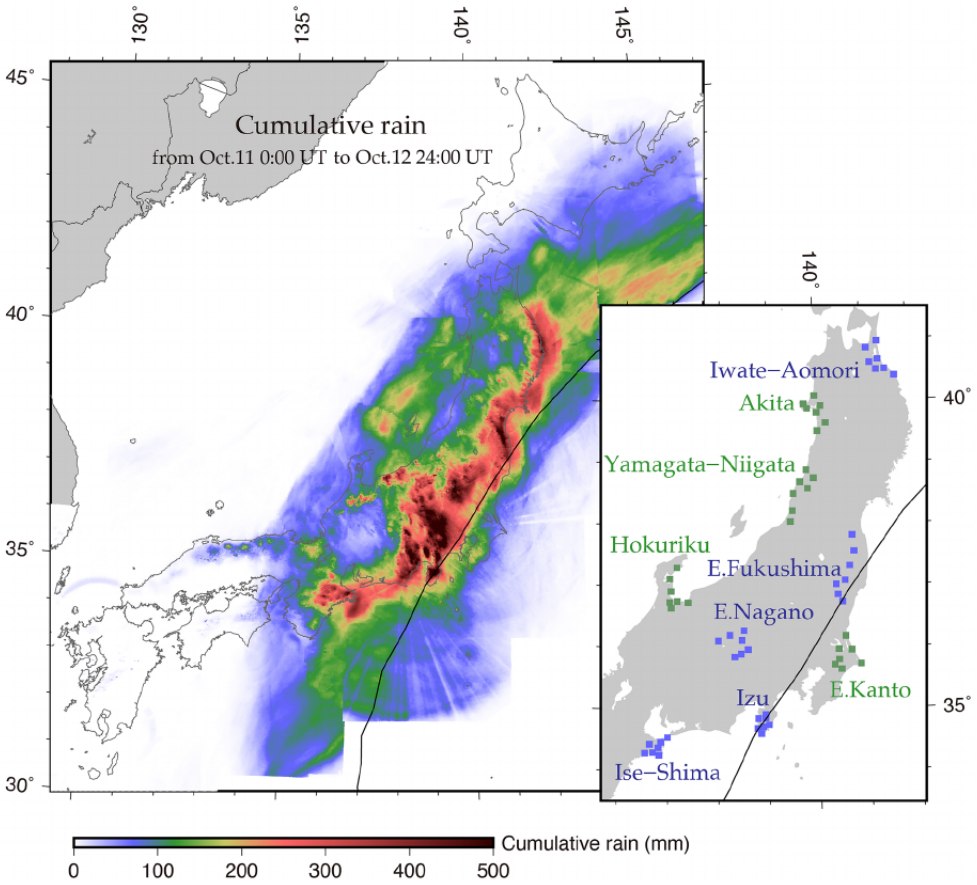

Figure 6. Cumulative precipitation over the two whole days October 11 and 12, 2019, when the typhoon Hagibis went through the eastern Honshu along its path (black curve). Blue squares and green squares in the inset represent stations in five flooded regions and four nonflooded regions, respectively, used in Figure 7. The total amount of rain obtained by spatially integrating precipitation, over both land and ocean, is ~92 and ~33 Gt fell onto eastern Honshu.

overlap with the heavy rain regions shown in Figure 6. There is a time lag of hours in the onset of the heavy rain (Figure 4), that is, it started earlier in southwest and later in northeast. However, time resolution of F5c is a day, and we are not able to see such time lags in Figure 7c.

Considering small and irregular shapes of flooded regions due to mountainous topography, horizontal displacements would not be so useful to infer distribution of surface loads. Figure S1 shows that there are more horizontal displacement signals on the day of the typhoon (Figure S1b) than on the previous and next days (Figures S1a and S1c). Nevertheless, it is difficult to see systematic distributions of horizontal displacements of GNSS stations on the typhoon landfall day. In this study, we only use vertical displacements. In the Section 4, we present a quantitative interpretation of the observed crustal subsidence.

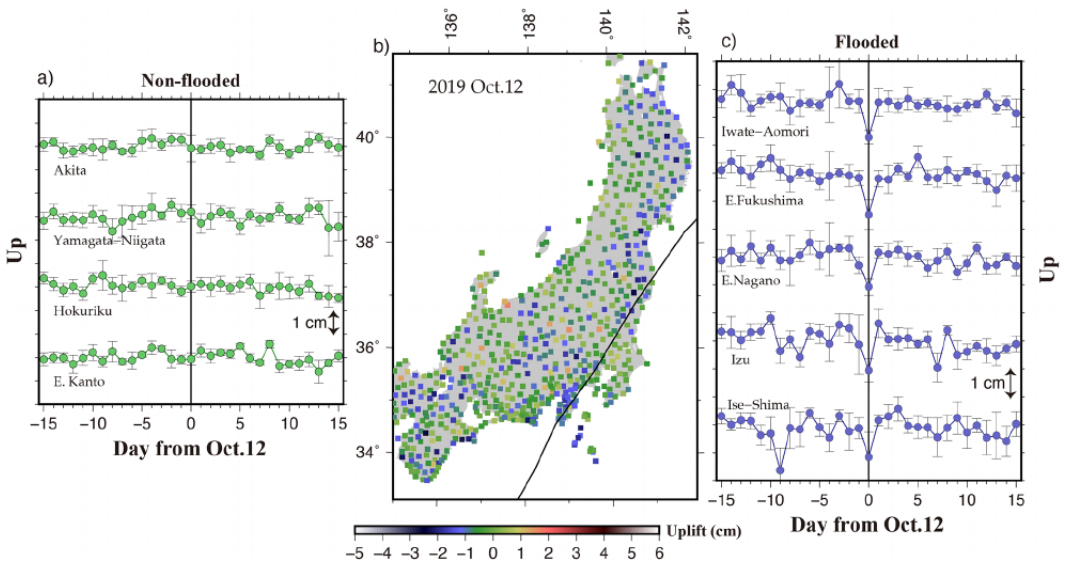

Figure 7. (a) Average time series of vertical coordinates of seven GNSS stations over a ±15 days period around October 12, 2019, located in four nonflooded areas (green symbols in Figure 6 inset). (b) Vertical displacement on October 12 relative to their reference positions (median of the ±15 days period). (c) Average time series of vertical coordinates of seven GNSS stations, located in five flooded areas (blue symbols in Figure 6 inset). Error bars in (a) and (c) reflect standard deviations of the daily vertical positions of seven stations within the groups.

4. Discussion

4.1. Temporal Evolution of Subsidence

In the case of the 2017 Hurricane Harvey, Milliner et al. (2018) reported water dissipated over a few weeks after the heavy rain. In the present case, however, crustal subsidence lasted for only a day (Figure 7c). Figure 8 compares daily maps of crustal subsidence from October 10 to October 14. There, we perform spatial smoothing, calculating averages using distance-dependent Gaussian weights with 20 km as the averaging

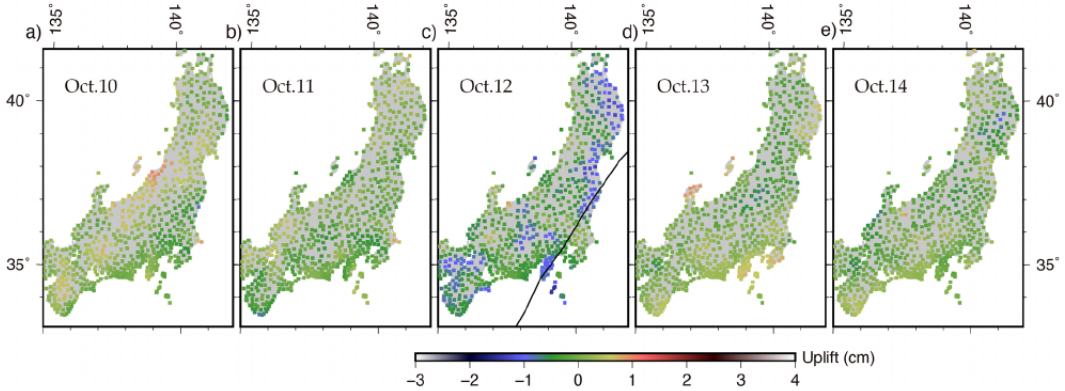

Figure 8. Crustal subsidence on five consecutive days, October 10–14, 2019, including October 12, the typhoon Hagibis landfall day (c). We see significant subsidence on October 12 along the typhoon path. On the next day (October 13), small amount of subsidence is seen in the inland region in Honshu. Spatial smoothing using 20 km as the averaging radius has been performed in all the panels.

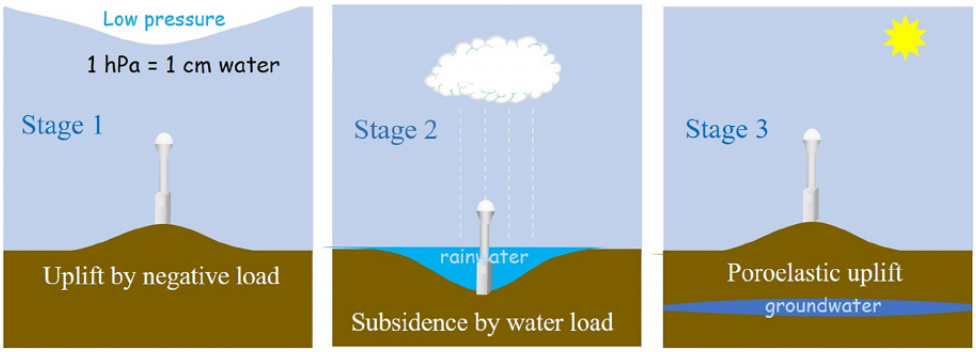

Figure 9. Three possible stages of typhoon-origin vertical crustal movements. First, atmospheric low pressure would cause crustal uplift by a negative load (Stage 1). Second, rainwater would depress the ground as a positive load (Stage 2). After surface water drained to the sea, groundwater may cause poroelastic uplift (Stage 3). The first two stages can be modeled as an elastic response of lithosphere to surface loads.

radius (Wahr et al., 1998). These figures clearly indicate that significant crustal subsidence took place only on the typhoon landfall day (October 12). Such subsidence recovered on the next day (October 13), although smaller amount of subsidence seems to have remained along the backbone range of the eastern Honshu. It is also obvious that subsidence was insignificant before the typhoon landfall (October 10 and 11).

In Figure S2, we show river water level anomalies at 17 water level gauges from October 5 to 20, 2019, made available from the Water Information System, Japan (www1.river.go.jp). Water levels show strong peaks on October 12. There is a difference between long (>200 km) (Figures Ss2a and S2b) and short rivers (Figures S2c and S2d). Short rivers show quick and narrow peaks within one day while long rivers often show enhanced water level lasting for a few days. Because the higher water level means an expansion of the river width, the water level is not proportional to the river flux. Therefore, the peak "flux" would be sharper than in Figure S2. As a whole, the river water level rapidly declines on October 13, indicating a substantial part of the rainwater has drained to the sea on that day. This is consistent with Figures 7c and 8, where large subsidence recovers quickly with little remnant subsidence on the later days.

4.2. Crustal Subsidence and Surface Load

4.2.1. Mechanisms of Vertical Crustal Movements in a Typhoon

In Figure 9, we show three possible stages in vertical crustal movements associated with a typhoon passage. At first, atmospheric low pressure of the typhoon would serve as a negative load and cause crustal uplift (Stage 1). This is to be followed by Stage 2, crustal subsidence by rain loads. Figure 8 does not show such a transition because rain started even before the typhoon landfall (Figure 4) making Stages 1 and 2 occur simultaneously. It is straightforward to correct for the crustal uplift in Stage 1 because its physical process is known (1 hPa atmospheric load corresponds to ~1 cm surface water). We here calculate the average surface pressure anomaly over the typhoon landfall day using the AMeDAS pressure data to correct for Stage 1 crustal uplift (Figure S3).

Poroelastic crustal uplift (Stage 3) due to the inflation of soil by groundwater would emerge as the surface water recharges groundwater. Water filling the pores in the silts, sands, and gravels of an aquifer cause solid Earth to expand and Earth's surface to rise, which is opposite the subsidence in an elastic response to the load of the water. It would occur with a certain time lag required for water to diffuse in the soil. In fact, GNSS stations in Izu seem to rise ~5 mm on October 13 (Figure 8d). However, we think it difficult to model such uplift with sufficient accuracy. In this study, we assume that this process is insignificant on the day of the typhoon landfall and neglect it.

We estimate surface load distribution assuming only Stages 1 and 2 using vertical crustal movement data on the typhoon landfall day. Then, we remove the atmospheric contribution using meteorological data

(Figure S3) from the estimated load. Figure 7a suggests that vertical crustal movements are insignificant for unflooded regions away from the typhoon path. This may not necessarily mean the lack of subsidence, that is, the positive rainwater load may have been canceled by the negative atmospheric load realizing the balance of Stages 1 and 2.

4.2.2. Estimation of Surface Load Distribution

Before estimating the load distribution, we need to confirm that surface loads exist only on land. Figure S4 compares the hourly values of two quantities, sea level anomalies and surface pressure anomalies, both from JMA. The sea level anomalies are derived by subtracting astronomical tides from observed tide gauge observations, and the sea-level atmospheric pressure anomalies are relative to 1 atm. Figure S4 indicates that negative pressure anomalies are well compensated by sea level uplift without noticeable time lag and deviation from expected amplitudes (−1 hPa anomaly makes 1 cm sea level rise). These observations enable us to assume no anomalous loads in oceanic areas, that is, atmospheric pressure is instantaneously compensated by sea level changes and rainwater from river mouths diffuses immediately to the Pacific Ocean.

We use crustal subsidence data from GNSS to estimate water load distribution using the Green's function for a spherical layered Earth given in Farrell (1972) following Argus et al. (2017). We set up 437 rectangular blocks covering the eastern Honshu land area. Each block has the size of 1/6° in longitude (~15 km) and 1/4° in latitude (~28 km), and we assume the load is uniform within a block (this may not be realistic as discussed later in Section 4.3). We employ rectangular blocks with north-south elongation because topographic features (mountain ranges and basins) generally run north-south in this region due to east-west plate convergence. Then, we estimate load in terms of equivalent water depth within individual blocks using subsidence data at 515 GNSS points on October 12, 2019 shown in Figure 7b. We assume that there are no load in the ocean.

To stabilize the solution, we apply continuity constraints. We simply assume that adjacent blocks have the same amounts of loads with a certain tolerance. Smaller tolerances realize strong constraints and smooth the estimated distributions. Here, we assume the error of vertical movements of GNSS stations as 5 mm (inter-software difference, see Figure 2) and employ the tolerance as 50 cm. This continuity constraint also applies for coastal blocks, that is, they are constrained around zero (because load is zero in the ocean) with the same tolerance. We use the subsidence of GNSS stations caused by a unit load in the individual blocks calculated using the Green's function in Farrell (1972) as the partial derivatives in the least squares inversion.

Correction of the atmospheric contribution can be made with two different methods. The first method is to correct vertical crustal movements caused by atmospheric pressure anomalies before inversion of the surface load distribution. In this method, it is important to use the same model for the crustal response to surface loads in the correction and the inversion. In this study, we employ the alternative approach that we remove atmospheric load from the inversion results assuming 1 hPa atmospheric pressure deficit equivalent to 1 cm depth water load. Because we use daily vertical positions for the input of the inversion, we averaged such pressure anomalies over Oct. 12 and interpolated the results for the 437 blocks as shown in Figure S3d.

Figure 10 shows the inversion results. The load distribution in Figure 10c best reproduces the observed vertical movements shown in Figure 10a. Figure 10b shows the vertical movements calculated using the estimated load distribution. The loads are mostly positive (blue color), with small but significant amount of negative loads (orange color). By subtracting the negative atmospheric load in Figure S3d from Figure 10c, such negative parts mostly disappear as seen in Figure 10d. The total amount of surface load becomes ~71 Gt, over twice as large as the precipitation onto these blocks shown in Figure 6. We call this discrepancy as "rainwater paradox" and discuss its origin in the next section.

4.3. Rainwater Paradox

4.3.1. Comparison Between Precipitation and Estimated Load

The amount of surface water necessary to explain the observed crustal subsidence (Figure 10a) significantly exceeds precipitation during the typhoon Hagibis passage (Figure 6). In fact, 33 Gt is the cumulative rain over the two days (October 11–12), and the average amount of water staying on ground surface on October

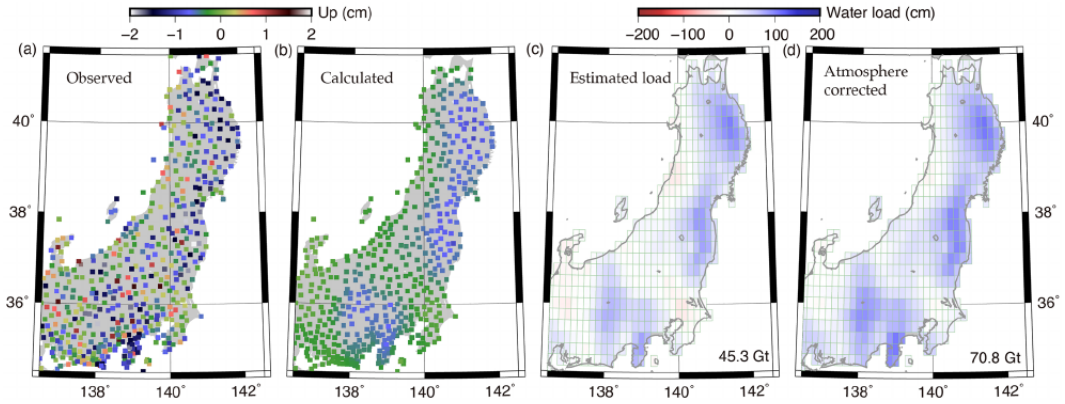

Figure 10. We set up 437 rectangular blocks with sizes of 1/6° in longitude and 1/4° in latitude covering eastern Honshu and estimated surface load by using vertical displacements of 515 stations within these blocks on October 12, 2019 (a). (b) Shows vertical movements calculated using the estimated distribution of load shown in (c). (d) Shows the load distribution after correcting atmospheric pressure anomalies given in Figure S3d. We used the Green's function for a realistic Earth given in Farrell (1972). We applied continuity constraint of 50 cm for adjacent blocks and assumed observation error as 5 mm. The total amount of surface water (sum of positive loads) is 45.3 Gt (c) and 70.8 Gt (d), which far exceeds precipitations within these blocks (~33 Gt) given in Figure 6.

12 should be smaller. Hence, the estimated load should not exceed the cumulative precipitation, and this discrepancy needs to be explained.

One might suspect the contribution of remnant water of rains before the typhoon. As explained earlier, there were no significant rainfalls during October 8–10 in eastern Honshu. The time series in Figure 7c shows that the subsidence emerged suddenly on October 12, suggesting that the typhoon rainwater is responsible for the subsidence. Others may suspect the contribution of rain load in oceanic area responsible for the subsidence of coastal stations, that is, neglecting this may let us overestimate loads on land. However, tide gauge stations do not show any extra sea level by rain as shown in Figure S4. Changing the block size and the continuity constraint in the inversion does not solve the discrepancy, either.

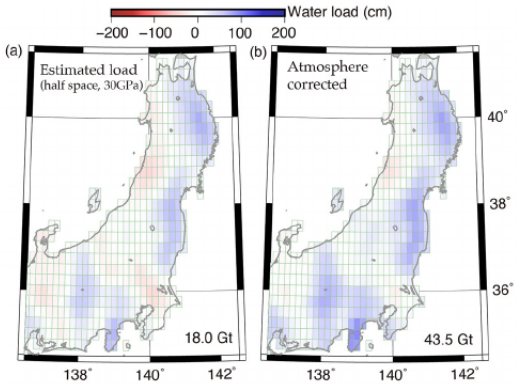

Figure 11. Same as Figures 10c and 10d, but we used the Farrell's (1972) model for the elastic response of a half-space to point loads assuming 30 GPa for rigidity and 0.25 for the Poisson's ratio. Other conditions of the inversion are the same as in Figure 10. Vertical movements calculated using the estimated load (a) are very similar to Figure 10b. (b) Shows the load distribution after applying the atmospheric pressure correction given in Figure S3d. The total amount of the surface water is now ~43.5 Gt after the atmospheric correction.

We hypothesize that two factors cause the discrepancy. The first factor is the smaller rigidity of ground beneath the GNSS stations. GEONET stations are installed within towns and cities on concrete basements installed deep in soil (not on bedrock). Rain load may exist as small patches and crustal subsidence may reflect rigidity of relatively shallow layers. A smaller rigidity of sedimentary rocks beneath them would cause more subsidence than calculated by the Green's function representing the whole earth, resulting in overestimation of rain loads. In Figure 11 we show the new inversion results obtained assuming elastic response of a half space to a point load given in Farrell (1972). Here we assume the half space with rigidity of 30 GPa, rigidity of typical crustal rocks. The load necessary to explain the observed subsidence decreased to ~44 Gt. Although this is still significantly more than the precipitation, we feel it inappropriate to further reduce the discrepancy by decreasing the rigidity. Instead, we propose the second factor for the discrepancy coming from topographic characteristics of the Japanese GNSS stations.

4.3.2. Topographic Feature of Japan and GEONET

Here, we discuss characteristics of the topography around the GEONET stations and propose the topographic amplification as the second factor responsible for the rainwater paradox. GNSS stations in Japan are

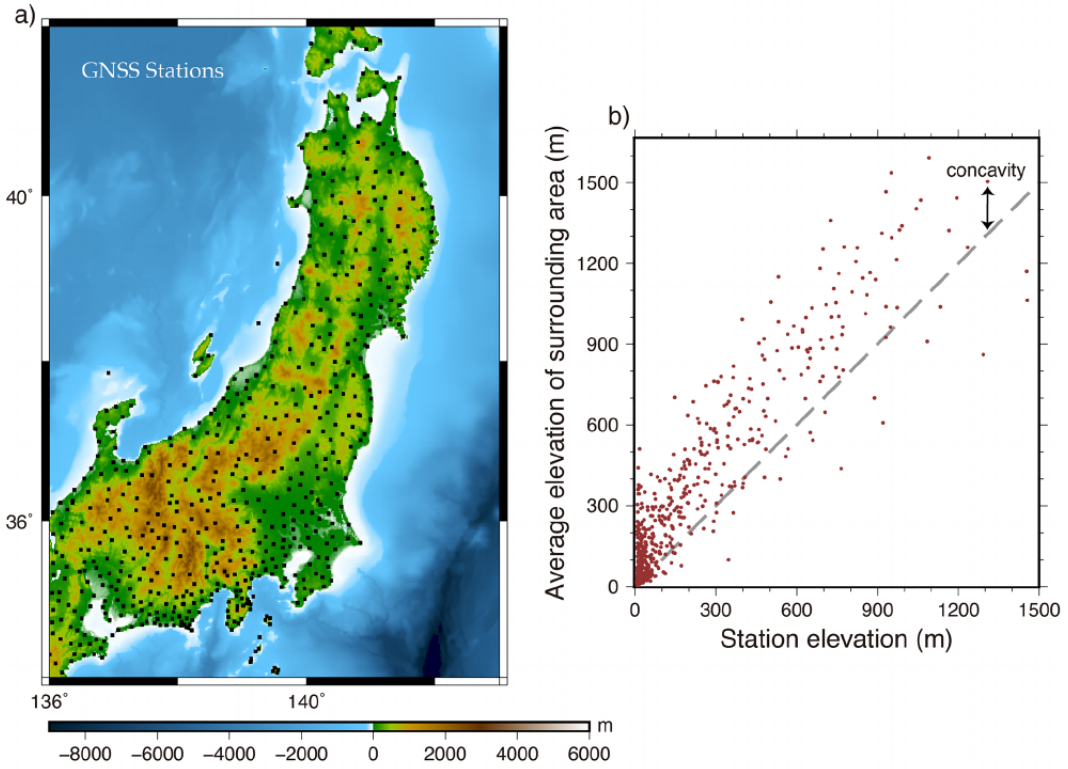

Figure 12. (a) Topography of eastern Honshu by the ETOPO1 model (Amante & Eakins, 2009) and the GEONET GNSS stations (black squares). In (b) we compare the elevation (height relative to geoid) in the horizontal axis, and the average elevation of the points within a rectangle covering ±10 km of the GNSS station. We define the difference between these two elevations as "concavity." Because ETOPO1 model has a resolution of 1/60°, one rectangle includes >100 points. Most of the GNSS stations are above the 45° line (flat terrain) indicating that the GNSS stations are located within concave terrains such as valleys or basins.

installed in cities and towns with significant population density because the stations rely on infrastructures like public electricity and communication lines. Japanese communities historically developed along valleys or within basins to secure water resource for growing rice, the staple food in Japan. Unlike snow, rainwater rapidly flows down the slope and gathers in such concave terrains. From this point of view, it would be unrealistic to assume uniform load within blocks as large as 15 × 28 km as in Figures 10 and 11. Water concentration around GNSS stations will cause extra subsidence and serious overestimation of surface water.

Here, we define the "concavity" of the terrane around GNSS station from a numerical topographic model. We use the Earth Topography One Minute Grid (ETOPO1) digital topography model with spatial resolution of 1 arcminute (Amante & Eakins, 2009) and compare the GNSS station heights and the average heights of the square ±10 km in north-south and in east-west around the station. We define the difference between the average height and the GNSS station height as the concavity and show them in Figure 12b. It indicates that most of the GNSS stations have positive concavity (typically 200–400 m), that is, they are mostly installed within concave terrains. Thus, the rainwater loads within individual blocks in Figures 10 and 11 would be highly nonuniform and concentrate around GNSS stations causing their extra subsidence. This situation is very different from the flat terrain around the Gulf of Mexico shown in Figure S5, where Milliner et al. (2018) studied crustal deformation caused by rainwater of the Hurricane Harvey in 2017.

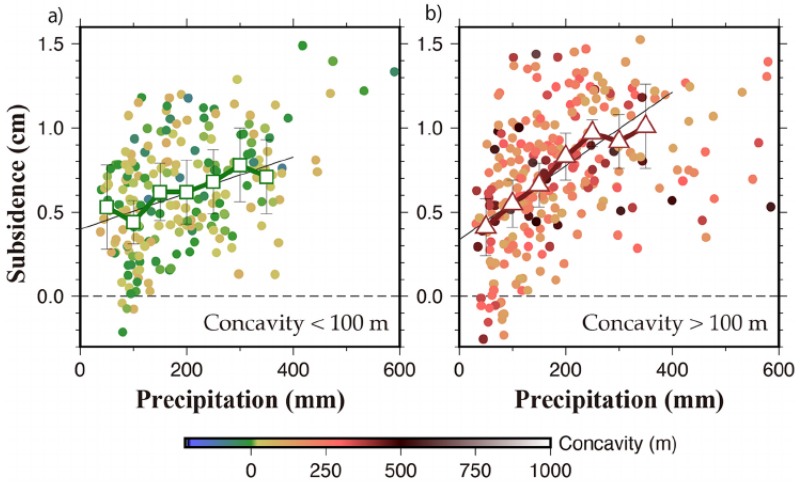

Figure 13. Diagrams showing the relationship between the precipitation (horizontal axis) and the subsidence after the atmospheric correction (vertical axis), for GNSS stations with various concavity of the surrounding terrains (shown with color). The stations are divided into two groups, those with concavity less than (a) and more than (b) 100 m. The squares in (a) and the triangles in (b) are the averages with their errors of values within 50 mm precipitation bins. We also show the best-fit linear functions for the data with precipitation <400 mm. The both groups show similar *y*-axis intercepts (subsidence for zero precipitation area), but the slope is about twice as large for the stations within very concave terrains (b) as for those within not-so-concave terrains (a).

4.3.3. Topographic Concavity and Overestimation of Water Loads

Figure 13 compares the three quantities for GNSS stations within eastern Honshu, subsidence, precipitation, and concavity. For the subsidence on October 12, 2019, we use spatially smoothed distribution of vertical displacements as shown in Figure 8c. We also correct for displacements caused by the atmospheric pressure anomalies shown in Figure S3d using the Green's function. As the precipitation, we use cumulative value over October11–12 from RRAP (Figure 6) at the closest grid points to the GEONET stations. We divide the GEONET points into two groups with their concavity, that is, the first group of stations are installed on relatively flat terrain (Figure 13a) and the second group of stations are built in highly concave terrains (concavity >100 m) (Figure 13b).

At a first glance, we see that they have large scatters reflecting diverse terrain conditions, proximity to large rivers, and others, of individual GNSS stations. Nevertheless, Figure 13 clearly shows positive correlations between subsidence and precipitation. They are nearly linear for the precipitation range 0–400 mm with *y*-axis intercept of ~4 mm, which means the subsidence at points with no precipitation. This would be partly because rainwater flows downstream even to regions without precipitation, and partly because the subsidence would extend to regions beyond the edge of the load (a "point" load makes "spherical" subsidence). Such a nonzero *y*-axis intercept would be the contribution of long-wavelength load, that is, the thin water load covering the whole eastern Honshu. Its large spatial coverage would have caused the subsidence of the whole eastern Honshu, including regions without precipitation.

We should note in Figure 13b that stations within highly concave terrains show more subsidence, that is, nearly twice as large (~0.22 cm for 100 mm precipitation) slope for precipitation as Figure 13a. This would be due to the rainwater concentration around the GNSS stations due to concave terrains, that is, the concavity doubled the sensitivity of crustal subsidence to precipitation. This qualitatively supports our hypothesis that concave terrains cause concentration of rainwater and extra subsidence of GNSS stations causing overestimation of the total amount of surface water with a factor of two or more.

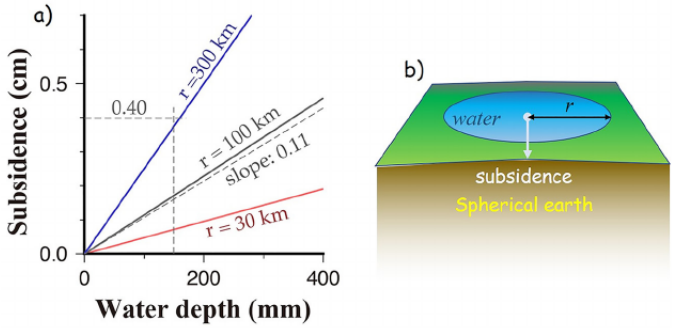

Figure 14. Subsidence of the point at the center of a circular water load as an elastic response of the layered spherical earth. A large disk makes more subsidence for a given water depth. The slope of the best-fit line observed in Figure 13a (~0.11 cm for 100 mm rainwater) corresponds to the slope of a circular water load with radius of ~100 km. The *y*-axis intercept in Figure 13a (subsidence for zero precipitation) corresponds to a crustal response of 300 km radius water load with thickness of ~150 mm.

We assume Figure 13a represents the elastic crustal response to water loads with only small concavity effects. Figure 14 shows results of a simple numerical experiment to interpret Figure 13a. We assume a disk load of water with various radii. A larger water radius increases the sensitivity of crustal subsidence to the water depth. The slope we observed in Figure 13a is ~0.11 cm for 100 mm precipitation, which corresponds to a water load with radius ~100 km. It is interesting to see in Figure 6 that the belt of extraordinary precipitation along the typhoon path (dark red zone in figure) has a width of a similar scale.

Another feature of Figure 13 is the uniform subsidence of ~4 mm for the entire eastern Honshu (*y*-intercept of the best-fit line). We think this reflects a large and thin water load. A close look of Figure 6 suggests that the whole region is covered by precipitation of 10–20 cm (blue-green-yellow region in Figure 6). The ~4 mm subsidence is realized by water depth of 15 cm of a disk with radius of 300 km, somewhat larger than the typical trench-normal width of the Japanese Islands. In short, the behavior of Figure 13a could be approximated as an overlapping contributions from two water loads with different scales, an extensive, stationary, thin, uniform water cover, and a moving patch of a small-scale thick water cover.

5. Conclusion and Future Perspective

In this study, we performed a comprehensive study of water brought by the typhoon Hagibis in Japan, 2019. We first reconstructed the distribution of altitude-corrected PWV on the typhoon landfall day (October 12). We could see the centroid of water vapor, moving together with the eye of the typhoon and the centroid of precipitation. We found the total amount of water vapor above the Japanese Islands ~20 Gt, which corresponds to the capacity of an atmospheric bucket transporting sea water to land.

The typhoon rainwater depressed the ground of a large part of eastern Honshu by up to 0.5–1.5 cm. We assume it was an elastic response of the lithosphere to surface load and estimated the total amount of water necessary to realize the observed subsidence. The Green's function for the spherical layered earth resulted in serious overestimation of water relative to precipitation. We considered the discrepancy partly coming from weaker crust beneath the GNSS stations, and replacement of the Green's function with the elastic response of a half space with rigidity of 30 GPa reduced the discrepancy.

The more important source for the discrepancy may have come from the topographic situation of the GNSS stations in Japan, that is, they are lower than surrounding terrains by a few hundreds of meters. Concave terrains around the stations let rainwater gather and cause extra subsidence of the GNSS stations. We confirmed this by comparing the relationship between precipitation and subsidence for GNSS stations with and without serious influences from the terrain concavity.

There are remaining issues out of the scope of the current study. One such issue would be to analyze crustal deformation with a higher temporal resolution. The UNR solutions provide station coordinates in higher time resolutions, although they are not so accurate as the daily coordinates. Future study of crustal subsidence/uplift in timescales shorter than a day would provide useful information on crustal dynamics on the typhoon landfall day. This will make it possible for us to utilize local scale hydrological models in the Japanese Islands and to study water budget of the typhoon rainwater, that is, consistency of the water flux such as precipitation, river runoff, evapotranspiration, and groundwater recharge as done by Milliner et al. (2018).

The evidence and discussion given in this study remain largely qualitative. In other words, the present study has not yet achieved quantitative consistency between the observed crustal subsidence and precipitation. We wish this study inspire followers to elucidate complicated crustal dynamics during heavy rains brought by tropical cyclones in mountainous countries.

Acknowledgments
The authors thank GSI (https://terras.gsi.go.jp/) and UNR (http://geodesy.unr.edu/) for providing GNSS position time series, JMA (https://www.jma.go.jp/jma/index.html) for RRAP data, and the Water Information System (https://www.river.go.jp/e/) for river water level data. This research was supported financially by the National Natural Science Foundation of China (Grant No. 41804010) and the National Key R & D Program of China (Grants 2018YFC1503606 and 2017YFC1500501) funded by the Ministry of Science, Technology of the People's Republic of China. W. Zhan was also supported by China Scholar Council as a visiting scholar while at Hokkaido University. The authors thank the editor P. Tregoning, the associated editor Y. Aoki, D. Argus and an anonymous reviewer for their constructive and detailed comments. Some figures are generated using the Generic Mapping Tools GMT (Wessel et al., 2013). The authors salute the people who struggle with natural disasters such as typhoons and COVID-19.

References

Amante, C., & Eakins, B. W. (2009). *ETOPO1 1 arc-minuteglobal relief model: Procedures, datasources andanalysis*(Vol. 24, pp. 19). NOAA Technical Memorandum NESDIS NGDC.

Argus, D. F., Landerer, F. W., Wiese, D. N., Martens, H. R., Fu, Y., Famiglietti, J. S., et al. (2017). Sustained water loss in California's mountain ranges during severe drought from 2012 to 2015 inferred from GPS. *Journal of Geophysical Research: Solid Earth, 122*, 10559–10585. https://doi.org/10.1002/2017JB014424

Arief, S., & Heki, K. (2020). GNSS meteorology for disastrous rainfalls in 2017–2019 summer in SW Japan: A new approach utilizing atmospheric delay gradients. *Frontiers of Earth Science, 8*, 182. https://doi.org/10.3389/feart.2020.00182

Bertiger, W., Bar-Sever, Y., Dorsey, A., Haines, B., Harvey, N., Hemberger, D., et al. (2020). GipsyX/RTGx, a new tool set for space geodetic operations and research. *Advances in Space Research, 66*, 469–489. https://doi.org/10.1016/j.asr.2020.04.015

Bevis, M., Businger, S., Herring, T. A., Rocken, C., Anthes, R. A., & Ware, R. H. (1992). GPS meteorology: Remote sensing of atmospheric water vapor using the Global Positioning System. *Journal of Geophysical Research*, *97*(D14), 15787–15801. https://doi.org/10.1029/92jd01517

Blewitt, G., Hammond, W. C., & Kreemer, C. (2018). Harnessing the GPS data explosion for interdisciplinary science. *Eos, Transactions, American Geophysical Union, 99*, 1–2. https://doi.org/10.1029/2018eo104623

Böhm, J., Werl, B., & Schuh, H. (2006). Troposphere mapping functions for GPS and very long baseline interferometry from European centre for medium-range weather forecasts operational analysis data. *Journal of Geophysical Research*, *111*, B02406. https://doi.org/10.1029/2005JB003629

Chen, G., & Herring, T. A. (1997). Effects of atmospheric azimuthal asymmetry on the analysis of space geodetic data. *Journalof Geophysical Research, 102*(B9), 20489–20502. https://doi.org/10.1029/97jb01739

Ejigu, Y. G., Teferle, F. N., Kos, A., Bogusz, J., & Hunegnaw, A. (2020). Tracking Hurricanes using GPS atmospheric integrated water vapor field. In *International Association o*ȷ*Geodesy Symposia* (pp. 1–9).

Farrell, W. E. (1972). Deformation of the Earth by surface loads. *Reviews of Geophysics*, *10*(3), 761–797. https://doi.org/10.1029/rg010i003p00761

Graffigna, V., Hernández-Pajares, M., Gende, M., Azpilicueta, F., & Antico, P. (2019). Interpretation of the tropospheric gradients estimated with GPS during Hurricane Harvey. *Earth and Space Science, 6*(8), 1348–1365. https://doi.org/10.1029/2018EA000527

Heki, K. (2001). Seasonal modulation of interseismic strain buildup in northeastern Japan driven by snow loads. *Science*, *293*, 89–92. https://doi.org/10.1126/science.1061056

Heki, K. (2004). Dense GPS array as a new sensor of seasonal changes of surface loads. In R.S.J. Sparks, & C.J. Hawkesworth (Eds.), The state of the planet: Frontiers and challenges in geophysics, *Geophysical Monograph Series*. (Vol. 150, pp. 177–196). AGU. https://doi.org/10.1029/150gm15

Milliner, C., Materna, K., Bürgmann, R., Fu, Y., Moore, A. W., Bekaert, D., et al. (2018). Tracking the weight of Hurricane Harvey's stormwater using GPS data. *Science Advances*, *4*(9), eaau2477. https://doi.org/10.1126/sciadv.aau2477

Nakagawa, H., Toyofuku, T., Kotani, K., Miyahara, B., Iwashita, C., Kawamoto, S., et al. (2009). Development and validation of GEONET new analysis strategy (Version 4). *Journal of the Geographical Survey Institute, 118*, 1–8.

Natsuaki, R., & Nagai, H. (2020). Synthetic aperture radar flood detection under multiple modes and multiple orbit conditions: A case study in Japan on Typhoon Hagibis, 2019. *Remote Sensing*, *12*(6), 903. https://doi.org/10.3390/rs12060903

Nippon Hoso Kyokai (NHK) (2019). *Typhoon Hagibis and its aftermath.* Retrieved from: https://www3.nhk.or.jp/nhkworld/en/news/special/01/1919

Petit, G., & Luzum, B. (Eds.), (2010). IERS conventions. *IERS Technical note 36*. Verlagdes Bundesamts für Kartographie und Geodäsie. Retrieved from http://tai.bipm.org/iers/conv2010/

Shoji, Y. (2015). Water vapor estimation using ground-based GNSS observation network and its application for meteorology. *Tenki*, *62*(12), 3–19.

Simmons, A., Uppala, S., Dee, D., & Kobayashi, S. (2007). ERAInterim: New ECMWF reanalysis products from 1989 onwards. *ECMWF Newsletter*, *110*, 25–35. https://doi.org/10.21957/pocnex23c6

Takamatsu, N., Muramatsu, H., Furuya, T., Abe, S., & Hiyama, Y. (2020). The development of the new analysis strategy of GEONET. Paper presented at the *2020 Fall Meeting of American Geophysical Union.* https://doi.org/10.1037/t77665-000

Tay, C. W. J., Yun, S.-H., Chin, S. T., Bhardwaj, A., Jung, J., & Hill, E. M. (2020). Rapid flood and damage mapping using synthetic aperture radar in response to Typhoon Hagibis, Japan. *Scientific Data, 7*(1), 1–9. https://doi.org/10.1038/s41597-020-0443-5

Tsuda, T., Heki, K., Miyazaki, S., Aonashi, K., Hirahara, K., Nakamura, H., et al. (1998). GPS meteorology project of Japan-Exploring frontiers of geodesy. *Earth Planets and Spac, 50*(10), i–v. https://doi.org/10.1186/bf03352172

Tsuji, H., Hatanaka, Y., & Hatanaka, Y. (2018). GEONET as infrastructure for disaster mitigation. *Journal of Disaster Research*, *13*(3), 424–432. https://doi.org/10.20965/jdr.2018.p0424

Wahr, J., Molenaar, M., & Bryan, F. (1998). Time variability of the Earth's gravity field: Hydrological and oceanic effects and their possible detection using GRACE. *Journal of Geophysical Research*, *103*, 30205–30229. https://doi.org/10.1029/98jb02844

Wessel, P., Smith, W. H. F., Scharroo, R., Luis, J., & Wobbe, F. (2013). Generic mapping tools: Improved version released. *Eos, Transactions American Geophysical Union*, *94*(45), 409–410. https://doi.org/10.1002/2013EO450001

Zhao, Q., Yao, Y., & Yao, W. (2018). GPS-based PWV for precipitation forecasting and its application to a typhoon event. *Journal of Atmospheric and SolarTerrestrial Physics*, *167*, 124–133. https://doi.org/10.1016/j.jastp.2017.11.013

Zumberge, J. F., Heflin, M. B., Jefferson, D. C., Watkins, M. M., & Webb, F. H. (1997). Precise point positioning for the efficient and robust analysis of GPS data from large networks. *Journal of Geophysical Research*, *102*, 5005–5017. https://doi.org/10.1029/96jb03860